Equatorial Pacific gravity lineaments: interpretations with basement topography along seismic reflection lines

Neil C. Mitchell[1] and Huw Davies[2]

[1]School of Earth and Environmental Sciences, University of Manchester, Williamson Building, Oxford Road, Manchester M13 9PL, UK.

[2]School of Earth and Ocean Sciences, Cardiff University, Main Building, Park Place, Cardiff CF10 3AT, UK.

Abstract
The central equatorial Pacific is interesting for studying clues to upper mantle processes, as the region lacks complicating effects of continental remnants or major volcanic plateaus. In particular, the most recently produced maps of the

free-air gravity field from satellite altimetry show in greater detail the previously reported lineaments west of the East Pacific Rise (EPR) that are aligned with plate motion over the mantle and originally suggested to have formed from mantle convection rolls. In contrast, the gravity field 600 km or farther west of the EPR reveals lineaments with varied orientations. Some are also parallel with plate motion over the mantle but others are sub-parallel with fracture zones or have other orientations.   This region is covered by pelagic sediments reaching ~500-600 m thickness so bathymetry is not so useful for seeking evidence for plate deformation across the lineaments. We instead use depth to basement from three seismic reflection cruises. In some segments of these seismic data crossing the lineaments, we find that the co-variation between gravity and basement depth is roughly compatible with typical densities of basement rocks (basalt, gabbro or mantle), as expected for some explanations for the lineaments (e.g., mantle convection rolls, viscous asthenospheric inter-fingering or extensional deformation). However, some other lineaments are associated with major changes in basement depth with only subtle changes in the gravity field, suggesting topography that is locally supported by varied crustal thickness. Overall, the multiple gravity lineament orientations suggest that they have multiple origins. In particular, we propose that a further asthenospheric inter-fingering instability mechanism could occur from pressure variations in the asthenosphere arising from regional topography and such a mechanism may explain some obliquely oriented gravity lineaments that have no other obvious origin.

Introduction

Haxby and Weissel (1986) discovered a series of lineaments in the marine gravity field recorded using satellite altimetry, forming elongated troughs and swells of 5-20 mGal amplitude spaced ~200 km in the Pacific and Indian Oceans. As the lineaments in the Pacific Ocean were parallel to the present plate movement over Earth's mantle and cross fracture zones ("cross-grain"), they were initially speculated to be caused by elongated small-scale convection rolls in the asthenospheric mantle, which were expected to develop within the first few million years (Buck and Parmentier 1986; Haxby and Weissel 1986). That convection would provide vertical stresses that initially distort the overlying lithosphere (Figure 1a), creating topography that becomes "frozen in" by the cooling plate. Subsequently, other authors have characterised and commented on these and larger similar features in satellite altimetry data (Baudry and Kroenke 1991; Cazenave et al. 1992; Fleitout and Moriceau 1992; Maia and Diament 1991; McAdoo and Sandwell 1989; Sandwell et al. 1995; Wessel et al. 1996) and the convection model has received renewed interest more recently (Ballmer et al. 2009; Harmon et al. 2006).

Other explanations for the gravity lineaments have been put forward. Winterer and Sandwell (1987) suggested that extension arising from lithospheric cooling (Turcotte and Oxburgh 1973) could explain en-echelon volcanic ridges found within the Pacific plate that are parallel to these gravity lineaments, with the lithosphere deforming in a boudinage manner (Figure 1b). Alternatively, extension could arise from far-field stresses caused by slab pull associated with the Pacific plate's subduction zones (Dunbar and Sandwell 1988). Goodwillie and Parsons (1992) used separations of fracture zones at different locations to assess plate extension in the South Pacific about the East

Pacific Rise (EPR), but ruled out significant extension as explaining lineaments there, a conclusion similarly reached by Gans et al. (2003). Gans et al. (2003) suggested instead that flexing of the lithosphere caused by varied cooling rates with depth (Figure 1c) could explain the gravity lineament spacings and amplitudes. Cormier et al. (2011) presented multibeam data showing faults that support the possibility of such extension of the Cocos plate.

To explain a correspondence between slow seismic velocities beneath seamount chains of an area of the southern East Pacific Rise, Weeraratne et al. (2007) and Holmes et al. (2007) suggested that a viscous inter-fingering could occur in asthenosphere affected by an off-axis mantle thermal anomaly. Essentially, buoyancy in asthenosphere off-axis causes it to rise towards the axis beneath the dipping lithospheric lid. Fingers of the mobile asthenosphere may explain volcanic seamount chains (Figure 1a) that do not age systematically as expected of traditional mantle hotspot origins (Ballmer et al. 2009).

One of the most recently released grids of the marine gravity field (Sandwell et al. 2014) shown in Figure 2b reveals the lineaments originally identified by Haxby and Weissel (1986). The greater resolution of this new grid reveals a finer structure immediately west of the East Pacific Rise than in the earlier altimeter data, with troughs and swells spaced as closely as ~20 km. Figure 3c (described later) shows a high-pass filtered version of the gravity data. In it, the lineaments west of the East Pacific Rise can be seen giving way westwards into a pattern of lineaments that is more confused though with three or more dominant orientations (red arrows annotated A-F), which we focus on here.

In this study, we take advantage of interpreted seismic reflection data from three research cruises (Bloomer et al. 1995; Dubois and Mitchell 2012; Eittreim et al. 1994; Gnibidenko et al. 1990) and a recent compilation of seafloor spreading anomalies (Barckhausen et al. 2013) to evaluate the extent to which basement relief varies with gravity anomalies across these lineaments, supporting some of the explanations for the lineaments that have been put forward. The model profiles shown in Figure 1 suggest that, as the upper surface of the plate is a major density contrast, its deformation by the various mechanisms should lead to gravity anomalies varying sympathetically by amounts expected of basement with a high density typical of mantle rocks. This assumes that the crust has uniform thickness so it contributes a nearly uniform amount to the gravity field. In practice, however, the crust may vary in thickness, in particular, where volcanism has been promoted (e.g., at locations marked "v?" in Figure 1), hence the comparison is not straightforward. As part of the work, we also re-evaluate the Pacific tectonic plate subsidence. Previous subsidence studies (Crosby and McKenzie 2009; Parsons and Sclater 1977; Trehu 1975) have tended to use gridded datasets (e.g., sediment thickness from seismic reflection data (Divins 2003; Ludwig and Houtz 1979; Whittaker et al. 2013)), where errors may have been possible due to incomplete sampling and reflective chert horizons (Mitchell 1998). The new results allow us to verify those earlier subsidence rates and locate where the seabed lies above or below those trends.

Data and methods

Seismic reflection data

Seismic reflection data were obtained during the AMAT03 cruise of RV *Revelle* in 2004, which was a site-survey cruise for IODP Expedition 320/321. Recordings were made with a 4-channel streamer towed at ~10 knots between sites and with a 48-channel streamer towed at ~6 knots at the drill sites. The seismic source comprised two 150 cubic inch generator-injector (GI) guns. A segment of the data is shown in Figure 4, illustrating the typical visibility of the basement reflection. The full dataset is too large to present here, though several images of the data covering >1000 km were shown by Tominaga et al. (2011) and Dubois and Mitchell (2012), and the full dataset can be obtained from the UTIG Academic Seismic Data Portal (http://www.ig.utexas.edu/sdc/).

The recorded seismic data were interpreted as described by Dubois and Mitchell (2012) (also see Mitchell and Dubois (2014)), including the basement reflection two-way time, which is plotted against ship tracks in Figure 5. To compute accurately the depth of the basement below the seabed from the interval two-way time t, allowance needs to be made for variations of seismic velocity with sediment depth because of compaction and diagenesis in these sediments (carbonate ooze). Mayer et al. (1985) estimated *in situ* velocity from logged core velocity data from the central equatorial Pacific, correcting mainly for loss of confining pressure. The velocity variation with depth (~1500 m s^{-1} at the surface to >2000 m s^{-1} below 400 metres below seafloor (mbsf)) was approximated with a linear trend, $V=V_0+Bz$, where z is depth below seabed, and coefficients V_0 and B found by least-squares regression (V_0= 1479 m s^{-1}; B= 1.0286 s^{-1}). The following equation derived by integration was used here to estimate z:

$$z = \frac{V_0}{B}\left(e^{Bt/2} - 1\right)$$

(1)

Equation (1) was used to calculate basement depth from the two-way time data derived from the AMAT03 seismic reflection data and the Venture-1 data of Bloomer et al. (1995) .

As described by Eittreim et al. (1994), the RV *Akademik Selskiy* data were collected with a 24-channel, 2400-m streamer with airgun arrays of 23 or 46 L and mostly shot with 24-fold along the line marked in Figure 2. After processing, the data revealed Moho, crustal and basement reflections. The seabed and basement reflection two-way times interpreted by Eittreim et al. (1994) were digitized and converted to depth using a sediment velocity of 1540 m s^{-1} typical of ODP Site 1219 measurements (Lyle et al. 2002) and a water velocity of 1500 m s^{-1}. Eittreim et al. (1994) also identified flat-lying Moho reflections and modestly dipping reflections in the lower crust. Two-way times from basement to the Moho reflections were converted to depth with a simplified oceanic velocity structure of an upper crust of constant 2.5 km thickness with velocity (V_p) of 5 km s^{-1} overlying a gabbro-dominated lower crust of varied thickness and velocity of 7 km s^{-1} (Mutter and Mutter 1993). A segment of the reflection interpretations are shown in Figure 6.

Magnetic anomaly identifications

Magnetic anomalies have been re-evaluated in this region by Barckhausen et al. (2013), exploiting the greater coverage provided by recent research vessel transits. One set of transits involved a vector magnetometer, which aided anomaly identifications in this low field area near the magnetic equator. The

density of identifications (red crosses in Figure 2a) was significantly improved compared with previous studies.

Crustal ages corresponding with their magnetic anomaly identifications and some of their isochrons around fracture zones were gridded using a surface-fitting program (Smith and Wessel 1990). Figure 2a shows age contours derived from that grid. The grid was then sampled along the seismic survey tracks to obtain crustal age at each seismic measurement. (Crustal age contours in Figure 2a do not perfectly honour the isochrons of Barckhausen et al. (2013) over the whole area, but the grid was constructed to match faithfully isochrons where they underlie the seismic ship tracks.) For the *Akademik Selskiy* data, crustal ages were similarly assigned using the isochrons of Barckhausen et al. (2013) and, where they were not available (<14 Ma and > 76 Ma), from the age grid of Müller et al. (2008).

Subsidence trends

Basement depths derived from the AMAT03, Venture-1 and *Akademik Selskiy* cruises were corrected for isostatic sediment loading using a sediment wet bulk density of 1.4 g cm^{-3} (a column-average of IODP core measurements (Lyle et al. 2002; Pälike et al. 2010)) and a mantle density of 3.3 g cm^{-3}. Those corrected depths are shown in Figures 7 and 8 versus the square root of seafloor age. Simple least-squares regressions of the data was used to find the subsidence rates, with that in Figure 8 calculated from data restricted to less than 8 Ma$^{1/2}$ where basement depths break from the subsidence trend. Basement elevation residuals about the regression lines of Figures 7 and 8 are

shown along-track in Figures 5 and 3 (these are residual elevations rather than residual depths as positive values lie above the regression line).

Gravity anomalies

Free air gravity anomalies were derived from satellite altimeter measurements (Sandwell and Smith 1997). The data shown in Figure 2b are from version 23 of the free-air anomaly grid available from http://topex.ucsd.edu/. According to Sandwell et al. (2014), this version has an average accuracy of ~2 mGal in deep water, with most of the improvement over earlier versions in the 12-40 km wavelength band and improved resolution of features to as small as 6 km.

For crust that is locally Airy supported, variations in basement topography have little effect on the free-air gravity field because topography is supported by thickened crust of lower density than the underlying mantle (i.e., the increased gravitational attraction from the elevated topography is almost balanced by the reduced attraction from the greater crustal root which displaces dense mantle rocks). However, short-wavelength topography can be supported by the rigidity of the lithosphere so it can affect the gravity field. Free-air anomalies that are high-pass filtered therefore reflect crustal density and topography variations, whereas low-pass filtered anomalies should reflect potential deeper mantle sources (non-Airy supported topography). Relevant to the filter length-scale required, according to Cochran (1979), the elastic thickness of the lithosphere is 2-6 km about the East Pacific Rise. Modelling by Smith (1998) suggests that little effect of crustal variations appear in the gravity field for spatial scales larger than 200 km for these elastic thicknesses. The

gravity field (Figure 2b) was therefore convolved with a cosine-tapered weight of 400 km full width (Wessel and Smith 1991), which contains most weight over 200 km distance. The result in Figure 3a was subtracted from the field (Figure 2) to produce the high-pass filtered gravity field in Figure 3b. Thus, Figure 3a is intended to represent deeper (mantle) sources, whereas Figure 3b should represent mainly lateral variations in basement topography, or crustal densities and thickness.

Line segments V1, A2, A4 and A7 located in Figure 2a run along crustal isochrons, so any effect of lithospheric thermal subsidence should be uniform along them. For discussion of variations of gravity with basement structure, Figure 9 shows cross sections of basement and seabed topography along with the unfiltered free-air anomaly sampled from the grid provided by Sandwell et al. (2014).

The free-air anomalies shown in Figure 9 are affected by the sediment-water density contrast at the seabed as well as the basement and deeper contrasts that we are primarily interested in. To reduce the effect of the seabed contrast, Bouguer gravity anomalies were calculated by adding the following quantity to the free-air gravity anomalies:

$$\Delta g = 2\pi G \Delta \rho h \qquad (2)$$

where G is the gravitational constant (6.6726 X 10^{-11} m^3 kg^{-1} s^{-2}), $\Delta\rho$ is the density contrast between seabed sediments and seawater and h is water depth. The formula accounts for the gravitational attraction of a layer of material of infinite extent and hence we use it assuming that the topography of the seabed is slowly varying laterally. The grid of Bouguer anomalies was filtered with a 400 km filter as described earlier for the free-air anomalies and the resulting residual

anomalies (effectively high-pass filtered) were sampled along the survey lines, producing the results shown by the red lines in Figure 9. Because the density contrast between sediments and seawater is small (only 0.4 g cm^{-3} based on average sediment density of 1.4 g cm^{-3} (Lyle et al. 2002; Pälike et al. 2010)), the correction is modest but it produces an improvement. E.g., FAA declines by a few mGal on average along profile A2 in Figure 9a but this is largely caused by the topography of the equatorial sediments and its effect is largely removed in the Bouguer anomaly shown.

The bathymetry grid of Ryan et al. (2009) was used for h. The grid has varied resolution depending on the distribution of the tracks of cruises contributing bathymetry, although the multibeam data from both the AMAT03 and Venture-1 cruises have been incorporated in the grid, so resolution is adequate for the Bouguer correction along those lines. Resolution is poorer along the RV *Akademik Selskiy* line. Bouguer anomalies computed using depths derived from the seismic data differed from those computed with the Ryan et al. (2009) grid with a root-mean-square (RMS) difference of 2.3 mGal. It was therefore decided to use the former Bouguer anomalies for comparison with the basement variations. High-pass filtered anomalies shown by the red line in Figure 6 were computed by fitting a 5th-order polynomial of Bouguer anomaly versus longitude and calculating residuals relative to that polynomial.

To help assessment of any co-variation between Bouguer anomalies and basement elevations, these data for each line are shown in Figure 10 (admittance plots), using the residual elevations about the subsidence trends for basement elevation (Figures 7 and 8). In these graphs, Bouguer anomalies are shown after removing the 400-km-filtered field, but the elevations have not been similarly

high-pass filtered. In the case of the *Akademic Silskiy* line, data were restricted to 113°W to 145°W to avoid influence of some features near the EPR visible in Figure 2b and the Line Islands Swell to the west. Data from the two segments of apparently co-varying basement elevation and Bouguer anomalies marked by horizontal grey lines in Figure 6 are shown with red and blue colour in this panel (see figure caption for details).

In admittance plots constructed as described above, we expect changes in basement elevation with associated crustal thickness variations (local Airy isostatic support) to form horizontal trends. On the other hand, deflections of basement caused by mechanisms such as shown in Figure 1 should lead to a local correlation of Bouguer anomaly with basement elevation and the gradient of the correlation trend should correspond with a density contrast of mantle rocks with the sediments, if the crust has uniform thickness and therefore contributes little (also note that the Bouguer correction in effect replaced water with sediment in terms of its effect on the gravity field, hence the contrast is with sediment). If topography of the basement is supported by the rigidity of the lithosphere (e.g., because of off-axis emplacement of seamounts or faulting), other correlations are possible and hence we provide model trends in Figure 10 for gabbro and basalt lithologies (3.0 and 2.7 g cm^{-3}) as well as mantle lithologies (3.3 g cm^{-3}). Complicating somewhat the interpretation, the long-wavelength variation in basement elevation caused potentially by large-scale mantle convection (Crosby and McKenzie 2009; Crosby et al. 2006) will spread out the data generally parallel to the horizontal axis (any gravity effect having been removed by the high-pass filtering). However, this spreading out of the data is useful as it helps visibility of trends due to basement relief in smaller segments of the data.

In order to confirm the seismically derived structure, while also providing a test for the approach of providing calculations using the Bouguer slab formula, model free-air anomalies (green line in Figure 6) were calculated for the *Akademik Selskiy* line where Moho depths are available by adding the gravity contributions (using equation (2)) of the water column, sediment and crust using densities of 1.0, 1.4, 3.0 and 3.3 g cm^{-3} for water, sediment, crust and mantle, respectively. The somewhat large 3.0 g cm^{-3} was used for the crust given that crustal seismic layer 3 (gabbro) dominates variations in seismic estimates of crustal thickness (Mutter and Mutter 1993), whereas the seismic layer 2 is more uniform and therefore variations in layer 2 thickness should have less affect on gravity field variations than variations in the gabbroic layer thickness. Minshull et al. (1998) derived similar densities of ~3.0 g cm^{-3} for lower oceanic crust using their ~7 km s^{-1} velocities from seismic refraction experiments and a relation of Christensen and Shaw (1970), which Minshull et al. (1998) suggested was accurate to within a few percent. As the deeper mantle density structure is unknown here, the resulting model was simply de-trended and then re-trended to the gradient of the observed free-air anomalies. The resulting model and data have a root-mean square difference of 2.3 mGal, which is similar to the ~2 mGal accuracy of the gravity grid (Sandwell et al. 2014). The small discrepancy could partly arise from inadequate modelling of the crustal densities (e.g., seamounts may have a lower density (Mitchell 2001)) and/or from the Bouguer slab formula approach, which does not account well for topographic relief and crustal structure away from each point of calculation along the profile.

Results and interpretation

In the following, we first characterize the large-scale systematic variations

before examining the variability due to the gravity lineaments and other (e.g.,

volcanic structures) superimposed on those major trends.

Subsidence trend

The subsidence rate obtained from the AMAT03 and Venture-1 data

(Figure 7) is 313 m m.y.$^{-1/2}$, which is similar to that of Marty and Cazenave

(1989) who found 329 m m.y.$^{-1/2}$ for the equatorial Pacific (their corridor 26). It

is also similar to the global average rate of 323-336 m m.y.$^{-1/2}$ of Korenaga and

Korenaga (2008), to the 307 m m.y.$^{-1/2}$ North Pacific rate of Hillier and Watts

(2005) and to the 320 m m.y.$^{-1/2}$ average rate for the Pacific of Crosby and

McKenzie (2009). The latter is perhaps surprising, as Crosby and McKenzie

(2009) selected depths where they coincided with free air anomaly magnitudes

less than 5 mGal, to reduce effects of mantle upwelling and downwelling on their

subsidence rates. The AMAT03 seismic lines cross a broad gravity low (114° to

123°W) but encroach on gravity highs in the west and east ends of the analysed

region (Figure 3a), so any effect of downwelling may be fortuitously

compensated by upwellings to leave a similar subsidence trend as Crosby and

McKenzie (2009) found.

The subsidence rate derived from the *Akademik Selskiy* dataset was 343 m

m.y.$^{-1/2}$, which is somewhat more rapid than the previous estimates outlined

above. This is perhaps surprising if we expect a dynamic effect associated with

the long-wavelength free-air anomalies in Figure 3, as the dataset spans ~30

mGal from a -20 mGal low in the east to nearly +10 mGal in the west. If the east

of the line were dynamically depressed by mantle downwelling, while the west of

the line were elevated by upwelling near the Line Islands swell, a reduced

apparent subsidence rate might be expected.

We initially calculated 2σ uncertainties for our regressions using

standard methods (Taylor 1982) and obtained values of 2 and 4 m m.y.$^{-1/2}$ for

Figures 7 and 8. These values are much smaller than for the other subsidence

rates quoted above, whose uncertainties were reported to be 61 m.y.$^{-1/2}$ (Marty

and Cazenave 1989), 22-23 m m.y.$^{-1/2}$ (Korenaga and Korenaga 2008), 21-29 m

m.y.$^{-1/2}$ (Hillier and Watts 2005) and 30 m m.y.$^{-1/2}$ (Parsons and Sclater 1977).

Our small nominal uncertainties arise from the large numbers of data

contributing to the regressions. However, adjacent depth values along survey

lines obtained by digitising the seismic data are not strictly speaking

independent of each other because of the finite length-scales of abyssal hills and

other features (Goff 1992). Furthermore, the seismic lines severely under-

sample basement across the region. Hence, true uncertainties will be larger.

However, these issues highlight problems with the earlier subsidence rates also,

as the authors have used interpolated datasets where the underlying variations

(e.g., sediment thickness) were not measured continuously and there was no

allowance made apparently for the strong averaging of some data that occurs

during gridding. We therefore suggest that uncertainties of subsidence trends

are not so well constrained in ours and in the other studies. The significance of

differences in subsidence rates between regions may in turn be difficult to

assess.

Residual elevations

The residual elevations of basement corrected for sediment loading derived from the seismic data have similar magnitudes and vary with a similar spatial pattern to those of Crosby et al. (2006), as shown in Figure 11. Larger positive relief is evident along line V1 and generally larger amplitudes occur along lines A2-A7 due to the new data resolving seamounts and other elevated features.

Relations between basement elevations and gravity anomalies

Basement elevations varying sympathetically with Bouguer anomalies

In some segments, the basement rises and falls sympathetically with the Bouguer anomalies, as would be expected from some of the origins of the gravity lineaments (Figure 1). This can be seen in line A2 (Figure 9a), where local gravity highs "a"-"e" mimic basement highs. The corresponding admittance plot for this line (see filtered data in red in Figure 10) contains trends that generally have lower graph-gradients than the trends expected with the various basement densities, although the anomalies in Figure 9a are small in extent so this may be due to upward continuation effects.

The graph for profile A3 in Figure 10 contains varied trends that could be compatible with basement densities smaller than 2.7 to larger than 3.3 g cm^{-3} (i.e., large gravity variations occur in Figure 9b with modest variations in basement elevation). In Figure 9a, profile A4 mostly does not show sympathetic behaviour, although anomaly "a" and the further anomaly immediately south of it along that line do show sympathetic variations. In the admittance plot (Figure 10) some trends for A4 are nearly parallel to the expected trends.

The graph for profiles A5 and A6 in Figure 10 mostly shows trends that are equal to or shallower than the 2.7 g cm^{-3} trend. That for A7 is more confused, though the profile in Figure 9a suggests some sympathetic variation.

The *Akademik Selskiy* data also contain two segments where there are basement-Bouguer correlations (marked "c" and "d" in Figure 6 and highlighted by grey bars). The corresponding graph in Figure 10 contains data segments with the expected gradients for basement densities.

Basement topography with little or no Bouguer anomaly variation

In a few segments of the data, we find basement elevated by a few hundred metres or more coinciding with subdued gravity anomalies. For example, at "c" in profile A5-A6 (Figure 9b), there is a basement high of a few 100 m with two extreme local highs (seamounts) that is associated with a weak Bouguer high of only ~4 mGal. At 1°N in profile A3, a similarly extreme relief is associated with a gravity low. At 5°N in profile A7, a basement high of >500 m is accompanied by negligible Bouguer anomaly.

These features are most likely caused by thickened crust underlying seamounts or groups of seamounts. Figure 12a shows seamounts occurring in bathymetry collected with multibeam sonars in the northerly parts of profiles A4-A7. In the *Akademik Selskiy* data, local basement highs EH1 and EH2 are also associated with subdued Bouguer anomalies (Figure 6). The Moho imaged seismically beneath EH1 appears to be 500-1000 m deeper than areas a few degrees of longitude either side of the high. There is less clearly local deepening of the Moho beneath EH2, though the Moho is noticeably shallower under the adjacent low EL2. (Although an explanation is unclear, EH2 interestingly

coincides with the change in Pacific plate motion indicated by the bend of the Hawaiian-Emperor seamount chain (Clague and Dalrymple 1987).)

In line A4 (Figure 9a), the basement declines by ~300 m on crossing the Galapagos FZ over a distance of ~200 km, but the Bouguer anomalies are little changed. This forms a transition to an important low L2 in residual elevation that is ~300-400 km across (Figure 3a). We modelled the change in free-air anomaly going over this fracture zone (arrow in Figure 9a for A4) using the gravity slab formula (equation (2)) with two different assumptions. The mean basement depth, bathymetry and free-air gravity anomaly were first calculated for each of -1° to 0° and for 1.5° to 2.5°N.

First, we assumed the basement variation is locally compensated by crustal thickness variations. The difference in averaged basement elevation between the two areas is 311 m. If that were Airy compensated, the crust is predicted to thin by 2383 m from 0.5°S to 2°N as illustrated in Figure 13. This value was derived using a simple isostatic calculation using mantle, crustal and water densities (ρ_m, ρ_c, ρ_w) of 3.3, 3.0 and 1.0 g cm^{-3}. The gabbroic layer was assumed to dominate crustal thickness variations so a nearly constant 2.5 km thick layer 2 (Mutter and Mutter 1993) does not contribute to the isostatic calculation and we use a gabbroic 3.0 g cm^{-3} density for the crust as explained earlier. Sediment isostatic effects were ignored. With these assumptions, the change in Moho depth ΔM is predicted from the change in basement depth ΔB to be

$$\Delta M = \Delta B \ (\rho_c - \rho_w)/(\rho_m - \rho_c) \qquad (3)$$

The green bar in Figure 9a shows the expected free air anomaly (free-air anomaly at 0.5°S plus change) computed using the gravity slab formula from the

changes in seabed, basement and Moho density interfaces (a 1.6 g cm^{-3} density was assumed for the sediments (Mayer and Theyer 1985)). The predicted anomaly is not much different from the free-air anomaly in the Sandwell et al. (2014) grid (blue circle at 2°N in Figure 9a).

Second, if the basement depth change instead arises without change in crustal thickness (topography not locally compensated), the effect on gravity is shown by the red bar in Figure 9a (free-air anomaly at 0.5°S plus change). This calculation involved applying the gravity slab formula to the change in seabed and basement density interfaces, applying a mantle 3.3 g cm^{-3} density to the basement change as the gravity effect of the crust would be uniform in this case. This model clearly does a worse job of predicting the free-air gravity variations. There appears therefore to be a significant thinning of the crust by ~2 km crossing the Galapagos FZ northwards.

Discussion

Large-scale variations

At the larger scale (Figure 3a), the residual elevations correlate poorly with the regional free-air gravity anomalies. For example, a residual elevation high EH1 lies over the lowest free-air anomalies (<20 mGal), whereas the lowest residual elevation EL2 is far from the gravity low. Crustal thickness variations also affect basement elevations, so analysis of long-wavelength residual elevations also requires a correction for crustal thickness (Hoggard et al. 2016; Hoggard et al. 2017).

We therefore derived a residual elevation for the *Akademik Silskiy* data instead using the same global subsidence rate of 324 m m.y.$^{-0.5}$ of Hoggard et al.

(2017) and with their procedure. Basement depths were corrected for the effects of crustal thickness variations using crustal and asthenospheric mantle densities of 3.0 and 3.3 g cm^{-3}. The results offset to a zero mean are shown by the pink line in Figure 6. Although closer to the large-scale variation observed in the free-air anomalies, this profile still does not reproduce the low in those anomalies. Whatever causes the regional gravity low, it is apparently not so straightforwardly linked here to a surface elevation change.

We have earlier highlighted the ~400 km extent of depressed residual elevation L2 along line A4 and that it appears to correspond with crust that is ~2 km thinner than to the south of the Galapagos FZ. Such a change is similar to the full variability of crustal thicknesses compiled by Chen (1992) from post-1970 seismic refraction data. This is an unusually large area of thinned crust created at a fast-spreading ridge. If the crust south of the fracture zone has a thickness more typical of average crust (~7 km (Mutter and Mutter 1993)), that north of the fracture zone has 5 km thick crust. If this were to have been created by an area of mantle that is unusually cold, modelling suggests the temperature anomaly could be ~25-30° (Brown and White 1994; Su et al. 1994). Such a localised mantle temperature anomaly with an abrupt southern boundary seems unlikely, however. We suggest this was created by a body of mantle that had been depleted by a prior melting event, e.g., lithospheric mantle earlier recycled into the mantle at a subduction zone.

Finer-scale variations

The graphs described above (Figures 6, 9, 10) suggest that the lineaments observed in the gravity field (Figure 3c) could potentially have arisen from a

local deformation of the plate, such as by the mechanisms illustrated in Figure 1.
Although the apparent densities are not resolved sufficiently well to address
their formation mechanisms, some aspects of the spatial pattern made by the
lineaments in Figure 3c support some mechanisms over others.

East of "F" in Figure 3c, lineaments are finely spaced and oriented WNW,
parallel with the recent motion of the Pacific plate over the mantle (Figure 3b).
Mantle small-scale convection likely takes a few million years to initiate (Buck
1985), so their initiation in Figure 3c very close to the EPR (within 20 km?)
suggests another origin. These are probably crustal structures (e.g., seamount
chains) created above melting anomalies that are fixed in the mantle (Fleitout
and Moriceau 1992). The finest 20 km scale of these lineaments equals the
spacing of P-wave velocity anomalies suggestive of mantle upwellings in a large-
scale seismic refraction experiment on the EPR between the Clipperton and
Siqueiros fracture zones (Toomey et al. 2007).

Immediately west of there, lineaments are oriented N060˚E (parallel with
arrow marked by "F" in Figure 3c) and have a wider spacing (>100 km). These
lineaments are shorter (up to ~500 km) than others in Figure 3c. As they lie
oblique to flowline directions (Figure 3b), their orientations are incompatible
with small-scale convection (Buck and Parmentier 1986; Haxby and Weissel
1986) or with plate contraction, which is expected to occur parallel to the ridge
(Cormier et al. 2011; Dunbar and Sandwell 1988; Gans et al. 2003; Winterer and
Sandwell 1987). Given the proximity of the area of elevated topography and
seamounts over the westward extension of the Siqueiros FZ (Figure 2a), we
speculate that the static component of pressure in the asthenosphere here could
be affected by this topography and the asthenosphere mobilised in a manner

somewhat like lower crustal channels proposed on continents (Beaumont et al. 2004; Clark and Royden 2000; Royden et al. 1997). The asthenosphere may then have been affected by viscous inter-fingering as suggested by Weeraratne et al. (2007), though here arising from topographic potential energy rather than the buoyancy from off-axis hotter mantle that they had suggested.

The elevation difference driving such an inter-fingering movement between the elevated region and that ∼500 km to the south is roughly 200-500 m (Figure 2a) so the excess lithostatic pressure in the asthenosphere would be 4-10 MPa (200-500 m times 2000 kg m^{-3} times 10 m s^{-2}). This is small compared with the lithostatic pressure driving lower crustal flow in mountain regions with elevation differences of many kilometres and with crustal rocks contrasting in density with air rather than water (e.g., 100 MPa for the 4 km altitude of the Tibetan Plateau). However, the depth-extent of weak rheology forming any potential asthenospheric channel could be ∼50-100 km or larger based on seismic velocity profiles (Harmon et al. 2011; Maggi et al. 2006; Weeraratne et al. 2007), compared with <30 km for lower crustal channels (Beaumont et al. 2004). Buck (1985) assumed an asthenosphere viscosity of 10^{18} Pa s, compared with lower viscosities of 10^{18}-10^{19} Pa s suggested to occur in the crustal channels (Beaumont et al. 2004; Clark and Royden 2000). Furthermore, the volume of asthenosphere moved to deform the plate by up to a few 100 m at most (Figure 9) would be less than that elevating orogens by kilometres.

Some lineaments with trend "C" in Figure 3c, which parallel fracture zones, may have arisen from spreading centre processes. From the above interpretation of the residual elevations in line A4 and the apparent continuation of elevation lows to line A3 to the east and possibly parts of A6 to the west

(Figure 3b), these may accompanied long-lived processes that led to thinner than normal crust for several million years, perhaps as long as 10 m.y. (Figure 2a). Further lineaments with this orientation can be observed in this spreading corridor to the west (144°-135°W) and south of the Clipperton FZ.

Those lineaments in Figure 3c appear to be cross-cut by lineaments with orientation "A", which lie parallel to the motion of the Pacific plate for the past 20 m.y. or longer (see flowline in Figure 3b). The lineament marked "A" appears to continue to the East Pacific Rise, where it has a finer structure, presumably in part due to the shallow water depth (smaller upward continuation effect). Further lineaments beneath the *Akademik Silskiy* line ("B" in Figure 3c) are oriented clockwise of those at "A", but are parallel with the direction of motion of the Pacific plate prior to 30 Ma (Figure 3b). Given this correspondence, small-scale convection may explain both sets of these lineaments (Buck and Parmentier 1986; Haxby and Weissel 1986). Alternative explanations involving crustal construction at the East Pacific Rise modified by melting anomalies that are fixed in the hotspot reference frame (Fleitout and Moriceau 1992) seem to be ruled out in this area by their continuation across fracture zones and other structures where crustal thickness is reduced.

Returning to the possibility of extension causing these features, unfortunately we have found the seismic reflection records are not adequate to resolve this, despite sediment up to 600 m thick in places (Mitchell and Lyle 2005; Mitchell et al. 2003). As the sediment is pelagic, it commonly drapes the underlying basement (Dubois and Mitchell 2012; Mitchell and Huthnance 2013; Tominaga et al. 2011), making fault or fold displacements difficult to separate from depositional geometry. Faults can also arise because of differential

compaction. Nevertheless, pelagic draping means that the seabed relief

commonly appears as an attenuated version of the underlying basement relief

(Figure 4). As shown in Figure 12, multibeam sonar data from this area clearly

show the abyssal hills originally created at the East Pacific Rise. At fracture

zones (such as the Galapagos FZ in Figure 12b), there can be transverse features,

but otherwise we have observed no clear evidence for faults crossing the abyssal

hills here that would arise if the gravity lineaments were caused by plate

extension (Cormier et al. 2011; Dunbar and Sandwell 1988; Gans et al. 2003;

Winterer and Sandwell 1987).

Further lineament "E" (Figure 3c) is neither parallel to adjacent fracture

zones, nor to flowline directions. This feature is ∼1000 km long. Some similarly

oriented features lie north of the Clipperton FZ also. If lithosphere was weak

along the fracture zone, it is unclear how feature "F" could have formed by

extension with this oblique orientation. By elimination, a viscous inter-fingering

mechanism (Weeraratne et al. 2007) seems the only viable explanation for these

lineament directions at present.

In summary, the diversity of lineament orientations is difficult to explain

by any single mechanism (Figurer 1). It seems likely that multiple processes

have created the gravity lineaments here, of which we favour spreading centre

processes, small-scale convection, viscous inter-fingering and melting anomalies

that are fixed in the mantle reference frame. The Pacific plate changed absolute

velocity from ∼0.5°/m.y. prior to 30 Ma to ∼0.9°/m.y. after 30 Ma (Wessel and

Kroenke 2008), though neither this nor the changes in direction of motion

marked in Figure 3b appear to correlate with any of these changes in lineament

style. Further progress on these issues would benefit from further deep-seismic data capable of mapping the Moho.

Conclusions

Pelagic sediments up to 600 m thick obscure basement in the equatorial Pacific, preventing a simple comparison of the gravity field with bathymetry data. Depths of basement were therefore derived from these three seismic reflection datasets that cross this region and combined with re-evaluated seafloor spreading magnetic anomalies (Barckhausen et al. 2013). After correction for sediment isostatic loading, these depths reveal a simple plate-cooling trend with a subsidence rate of 313 m m.y.$^{-1/2}$ south of the Clipperton FZ (AMAT03 and Venture-1 datases) and 343 m m.y.$^{-1/2}$ immediately north of it (*Akademik Selskiy* dataset). These rates are broadly consistent with results of previous studies of this area that had been based on interpolated datasets.

Bouguer anomalies were computed from free-air gravity anomalies using the slab formula to correct for the seabed density contrast. The resulting anomalies in some places do not vary with basement topography, suggesting areas of crustal thickness variation, such as around seamounts. In other areas, however, basement topography varies in a similar way to that noted from bathymetry datasets elsewhere over gravity lineaments, forming low relief (100s of m) swells over ~100 km or smaller length-scales. Bouguer gravity anomalies vary over these features with an apparent basement density that varies, but includes 2.7-3.3 g cm^{-3} densities expected of basalt to mantle lithologies.

The gravity lineaments in the equatorial Pacific have remarkably varied orientations. Some are oriented parallel to Pacific plate flow-lines, changing

direction north of the Clipperton FZ, as expected from the different plate direction prior to 30 Ma if a mechanism such as small-scale convection formed them. However, other lineaments are oriented with directions that are not explainable by plate motion, so they require other mechanisms to be considered, such as viscous inter-fingering in the asthenosphere. Despite the thick sediment, the fine-scale abyssal hill morphology is commonly observed because the sediment is pelagic and tends to drape the underlying basement. We note that there are very few indications of faults crossing the abyssal hills that might be expected if the gravity lineaments were produced by extension.

Our detailed investigation has highlighted an area ~400 km across where residual basement elevations are unusually depressed. From a simple Airy isostatic argument, oceanic crust in this area is ~2 km thinner than outside the area. We suggest that this thin crust was created at the EPR for a period when the ridge overlay depleted mantle.

Acknowledgements

References

Ballmer MD, Hunen Jv, Ito G, Bianco TA, Tackley PJ (2009) Intraplate volcanism with complex age-distance patterns: A case for small-scale sublithospheric convection. Geochem. Geophys. Geosys. 10:article Q06015, doi:06010.01029/02009GC002386

Barckhausen U, Bagge M, Wilson DS (2013) Seafloor spreading anomalies and crustal ages of the Clarion-Clipperton Zone. Mar. Geophys. Res. 34:79-88

Baudry N, Kroenke L (1991) Intermediate-wavelength (400-600 km), South Pacific geoidal undulations: their relationship to linear volcanic chains. Earth Planet Sci. Lett. 102:430-443

Beaumont C, Jamieson RA, Nguyen MH, Medvedev S (2004) Crustal channel flows: 1. Numerical models with applications to the tectonics of the Himalayan-Tibetan orogen. J. Geophys. Res. 109:article B06406, doi:06410.01029/02003JB002809

Bloomer SF, Mayer LA, Moore TC (1995) Seismic stratigraphy of the eastern equatorial Pacific Ocean: Paleoceanographic implications. In: Pisias NG, Mayer LA, Janecek TR, Palmer-Julson A, van Andel TH (eds) Proceedings of the Ocean Drilling Program, Scientific Results, Vol. 138. Ocean Drilling Program, College Station, TX, pp 537-553

Brown JW, White RS (1994) Variation with spreading rate of oceanic crustal

thickness and geochemistry. Earth Panet. Sci. Lett. 121:435-449

Buck WR (1985) When does small-scale convection begin beneath oceanic lithosphere? Nature 313:775-777

Buck WR, Parmentier EM (1986) Convection beneath young oceanic lithosphere: Implications for thermal structure and gravity. J. Geophys. Res. 91:1961-1974

Cazenave A, Houry S, Lago B, Dominh K (1992) GEOSAT-derived geoid anomalies at medium wavelength. J. Geophys. Res. 97:7081-7096

Chen YJ (1992) Oceanic crustal thickness versus spreading rate. Geophys. Res. Lett. 19:753-756

Christensen NI, Shaw GH (1970) Elasticity of mafic rocks from the Mid-Atlantic Ridge. Geophysical J. Roy.l Astr. Soc. 20:271-284

Clague DA, Dalrymple GB (1987) Geologic evolution of the Hawaiian Emperor volcanic chain. In: Decker RW, Wright TL, Stauffer PH (eds) Volcanism in Hawaii, U. S. Geol. Surv. Prof. Paper 1350. U. S. Geological Survey, pp 85-100

Clark MK, Royden LH (2000) Topographic ooze: Building the eastern margin of Tibet by lower crustal flow. Geology 28:703-706

Cochran J, R. (1979) An analysis of isostasy in the worlds oceans 2. Mid-ocean ridge crests. J. Geophys. Res. 84(B9):4713-4729

Cormier MH, Gas KD, Wilson DS (2011) Gravity lineaments of the Cocos Plate: Evidence for a thermal contraction crack origin. Geochem. Geophys. Geosys. 12:article Q07007, doi:07010.01029/02011GC003573

Crosby AG, McKenzie D (2009) An analysis of young ocean depth, gravity and global residual topography. Geophys. J. Int. 178:1198-1219

Crosby AG, McKenzie D, Sclater JG (2006) The relationship between depth, age and gravity in the oceans. Geophys. J. Int. 166:553-573

Divins DL (2003) Total Sediment Thickness of the World's Oceans & Marginal

    Seas. In: Center NNGD (ed), Boulder, CO

Dubois N, Mitchell NC (2012) Large-scale sediment redistribution on the

    equatorial Pacific seafloor. Deep-Sea Res. I. 69:51-61

Dunbar J, Sandwell DT (1988) A boudinage model for cross- grain lineations

    (abstract). Eos Trans. AGU, 69:1429

Eittreim SL, Gnibidenko HS, Helsley CE, Sliter R, Mann D, Ragozin N (1994)

    Oceanic crustal thickness and seismic character along a central Pacific

    transect. J. Geophys. Res. 99:3139-3145

Fleitout L, Moriceau C (1992) Short-wavelength geoid, bathymetry and the

    convective pattern beneath the Pacific Ocean. Geophys J. Int. 110:6-28

Gans KD, Wilson DS, Macdonald KC (2003) Pacific Plate gravity lineaments:

    Diffuse extension or thermal contraction? Geochem. Geophys. Geosys.

    4(article 1074, doi:10.1029/2002GC000465)

Gnibidenko HS, Eittreim SL, Helsley CE, McClellan P, Ryan HF (1990) The Central

    Pacific Transect; cruise report of the research vessel Akademik Selskiy. U. S.

    Geol. Surv. Open-File Rept 90-532:1-13

Goff JA (1992) Quantative Characterstics of Abyssal Hill Morphology along flow

    line in the Atlantic Ocean. Journal of Geophysical Research 97(B6):9183-9202

Goodwillie AM, Parsons B (1992) Placing bounds on lithospheric deformation in

    the central Pacific ocean. Earth. Planet. Sci. Letts. 111:123-139

Harmon N, Forsyth DW, Scheirer DS (2006) Analysis of gravity and topography

    in the GLIMPSE study region: Isostatic compensation and uplift of the Sojourn

    and Hotu Matua Ridge systems. J. Geophys. Res. 111:article B11406,

    doi:11410.11029/12005JB004071

Harmon N, Forsyth DW, Weeraratne DS, Yang Y, Webb SC (2011) Mantle heterogeneity and off axis volcanism on young Pacific lithosphere. Earth Panet. Sci. Lett. 311:306-315

Haxby WF, Weissel JF (1986) Evidence for small-scale mantle convection from Seasat altimeter data. J. Geophys. Res. 91:3507-3520

Hillier JK, Watts AB (2005) Relationship between depth and age in the North Pacific Ocean. J. Geophys. Res. 110:article B02405, doi:02410.01029/02004JB003406

Hoggard MJ, White N, Al-Attar D (2016) Global dynamic topography observations reveal limited influence of large-scale mantle flow. Nat. Geosci. 9:456-463

Hoggard MJ, Winterbourne J, Czarnota K, White N (2017) Oceanic residual depth measurements, the plate cooling model, and global dynamic topography. J. Geophys. Res. 122:2328-2372

Holmes RC, Webb SC, Forsyth DW (2007) Crustal structure beneath the gravity lineations in the Gravity Lineations, Intraplate Melting, Petrologic and Seismic Expedition (GLIMPSE) study area from seismic refraction data. J. Geophs. Res. 112:article B07316, doi:07310.01029/02006JB004685

Korenaga T, Korenaga J (2008) Subsidence of normal oceanic lithosphere, apparent thermal expansivity, and seafloor flattening. Earth Planet. Sci. Lett. 268:41-51

Ludwig WJ, Houtz RE (1979) Isopach map of the sediments in the Pacific Ocean Basin, color map with text. In: Am. Assoc. Pet. Geol., Tulsa, OK

Lyle MW, Wilson PA, et_al. (2002) Leg 199 preliminary report, Paleogene Equatorial Transect, 23 October-16 December 2001. Ocean Drilling Program, College Station, TX

Maggi A, Debayle E, Priestley K, Barruol G (2006) Multimode surface waveform
    tomography of the Pacific Ocean: a closer look at the lithospheric cooling
    signature. Geophys. J. Int. 166:1384-1397

Maia M, Diament M (1991) An analysis of the altimetric geoid in various
    wavebands in the Central Pacific Ocean: constraints on the origin

of intraplate features. Tectonophys. 190:133-153

Marty JC, Cazenave A (1989) Regional variations in subsidence rate of oceanic
    plates: a global analysis. Earth Planet. Sci. Lett. 94:301-315

Mayer L, Theyer F (1985) Init. Repts. DSDP, 85. U. S. Govt. Printing Office,
    Washington

Mayer LA, Shipley TH, Theyer F, Wilkens RH, Winterer EL (1985) Seismic
    modeling and paleoceanography at Deep Sea Drilling Project Site 574. In:
    Mayer L, Theyer F, al. e (eds) Init. Repts. DSDP. U. S. Govt. Printing Office,
    Washington, DC, pp 947-970

McAdoo DC, Sandwell DT (1989) On the source of cross-grain lineations in the
    central Pacific gravity field. J. Geophys. Res. 94:9341-9352

Minshull TA, Bruguier NJ, Brozena JM (1998) Ridge-plume interactions or mantle
    heterogeneity near Ascension Island? Geology 26:115-118

Mitchell NC (1998) Modeling Cenozoic sedimentation in the central equatorial
    Pacific and implications for true polar wander. J. Geophys. Res. 103:17749-
    17766

Mitchell NC (2001) The transition from circular to stellate forms of submarine
    volcanoes. J. Geophys. Res. 106:1987-2003

Mitchell NC, Dubois N (2014) Evaluating Cenozoic equatorial sediment
    deposition anomalies for potential paleoceanographic and Pacific plate

motion applications. Marine Geophysical Research 35:1-20

Mitchell NC, Huthnance JM (2013) Geomorphological and geochemical evidence (^{230}Th anomalies) for cross-equatorial currents in the central Pacific. Deep-Sea Res. I. 78:24-41

Mitchell NC, Lyle MW (2005) Patchy deposits of Cenozoic pelagic sediments in the central Pacific. Geology 33:49-52

Mitchell NC, Lyle MW, Knappenberger MB, Liberty LM (2003) The Lower Miocene to Present stratigraphy of the equatorial Pacific sediment bulge and carbonate dissolution anomalies. Paleoceanography 18:DOI: 10.1029/2002PA000828

Müller RD, Sdrolias M, Gaina C, Roest WR (2008) Age, spreading rates, and spreading asymmetry of the world's ocean crust. Geochem. Geophys. Geosyst., 9:paper Q04006, doi:04010.01029/02007GC001743

Mutter CZ, Mutter JC (1993) Variations in thickness of layer 3 dominate oceanic crustal structure. Earth Planat. Sci. Lett. 117:295-317

Pälike H, Lyle M, Nishi H, Raffi I, Gamage K, Klaus A, the_Expedition_320/321_Scientists (2010) Proceedings of the Integrated Ocean Drilling Program, Volume 320/321. Integrated Ocean Drill. Program, College Station, Tex., doi:10.2204/iodp.proc.320321.320101.322010

Parsons B, Sclater JG (1977) An analysis of the variation of ocean floor bathymetry and heat flow with age. J. Geophys. Res. 82:803-827

Royden LH, Burchfiel BC, King RW, Wang E, Chen Z, Shen F, Liu Y (1997) Surface deformation and lower crustal flow in eastern Tibet. Science 276:788-790

Ryan WBF, Carbotte SM, Coplan JO, O'Hara S, Melkonian A, Arko R, Wiessel RA, Ferrini V, Goodwillie A, Nitsche F, Bonczkowski J, Zemsky R (2009) Global

multi-resolution topography synthesis. Geochem. Geophys. Geosys. 10:Paper Q03014

Sandwell D, Müller RD, Smith WHF, Garcia E, Francis R (2014) New global marine gravity model from CryoSat-2 and Jason-1 reveals buried tectonic structure. Science 346:65-67

Sandwell DT, Smith WHF (1997) Marine gravity anomaly from Geosat and ERS-1 satellite altimetry. J. Geophys. Res. 102:10039-10054

Sandwell DT, Winterer EL, Mammerickx J, Duncan RA, Lynch MA, Levitt DA, Johnson CL (1995) Evidence for diffuse extension of the Pacific plate from Pukapuka ridges and cross-grain gravity lineations. J. Geophys. Res. 100:15087-15099

Smith WHF (1998) Seafloor tectonic fabric from satellite altimetry. Annual Reviews in Earth and Planetary Sciences 26:697-738

Smith WHF, Wessel P (1990) Gridding with continuous curvature splines in tension. Geophysics 55(3):293-305

Su W, Mutter CZ, Mutter JC, Buck WR (1994) Some theoretical predictions on the relationships between spreading rate, mantle temperature, and crustal thickness. J. Geophys. Res. 99:3215-3227

Taylor JR (1982) An introduction to error analysis, The study of uncertainties in physical measurements. Oxford University Press, Mill Valley, California, p 270

Tominaga M, Lyle M, Mitchell NC (2011) Seismic interpretation of pelagic sedimentation regimes in the 18–53 Ma eastern equatorial Pacific: Basin-scale sedimentation and infilling of abyssal valleys. Geochem. Geophys. Geosys. 12:Paper Q03004, doi:03010.01029/02010GC003347

Toomey DR, Jousselin D, Dunn RA, Wilcock WSD, Detrick RS (2007) Skew of

mantle upwelling beneath the East Pacific Rise governs segmentation. Nature 446:409-414

Trehu AM (1975) Depth versus age: A perspective on mid-ocean rises. Earth Planet. Sci. Lettr. 77:287-304

Turcotte DL, Oxburgh ER (1973) Mid-plate tectonics. Nature 244:337-339

Weeraratne DS, Forsyth DW, Yang Y, Webb SC (2007) Rayleigh wave tomography beneath intraplate volcanic ridges in the South Pacific. J. Geophys. Res. 112:article B06303, doi:06310.01029/02006JB004403

Wessel P, Kroenke LW (2008) Pacific absolute plate motion since 145 Ma: An assessment of the fixed hot spot hypothesis. J. Geophys. Res. 113:Paper B06101, doi:06110.01029/02007JB005499

Wessel P, Kroenke LW, Bercovici D (1996) Pacific Plate motion and undulations in geoid and bathymetry. Earth Planet. Sci. Letts. 140:53-66

Wessel P, Smith WHF (1991) Free software helps map and display data. Eos, Transactions, American Geophysical Union 72:441

Whittaker JM, Goncharov A, Williams SE, Müller RD, Leitchenkov G (2013) Global sediment thickness data set updated for the Australian-Antarctic Southern Ocean. Geochem. Geophys. Geosys. 14:doi:10.1002/ggge.20181

Winterer EL, Sandwell DT (1987) Evidence from en-echelon cross-grain ridges for tensional cracks in the Pacific plate. Nature 329:534-537

Figures:

a) Small-scale convection or viscous interfingering

V?

Lithosphere

Asthenosphere

b) Boudinage

V?   V?

c) Thermal contraction

V?   V?
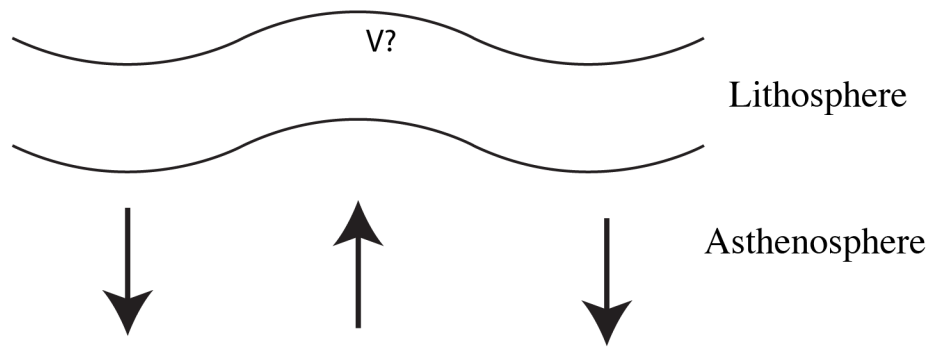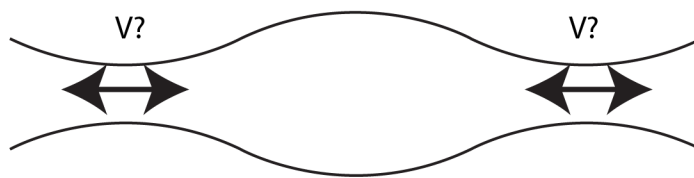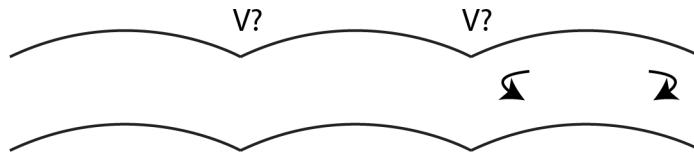
Figure 1. Some explanations for the gravity lineaments. (a) Vertical stresses (arrows) caused by small-scale convection (Buck and Parmentier 1986; Haxby and Weissel 1986) or viscous inter-fingering in the asthenosphere (Holmes et al. 2007; Weeraratne et al. 2007) deform the lithosphere. (b) Extension leads to boudinage of the lithosphere (Winterer and Sandwell 1987). (c) Thermal contraction increases with depth in the plate, creating a torque that buckles the lithosphere (Cormier et al. 2011; Gans et al. 2003). Volcanic edifices ("V?") can be emplaced at locations of extension lying in basement valleys in (b) and (c) but at highs overlying hot asthenosphere in (a).

a:
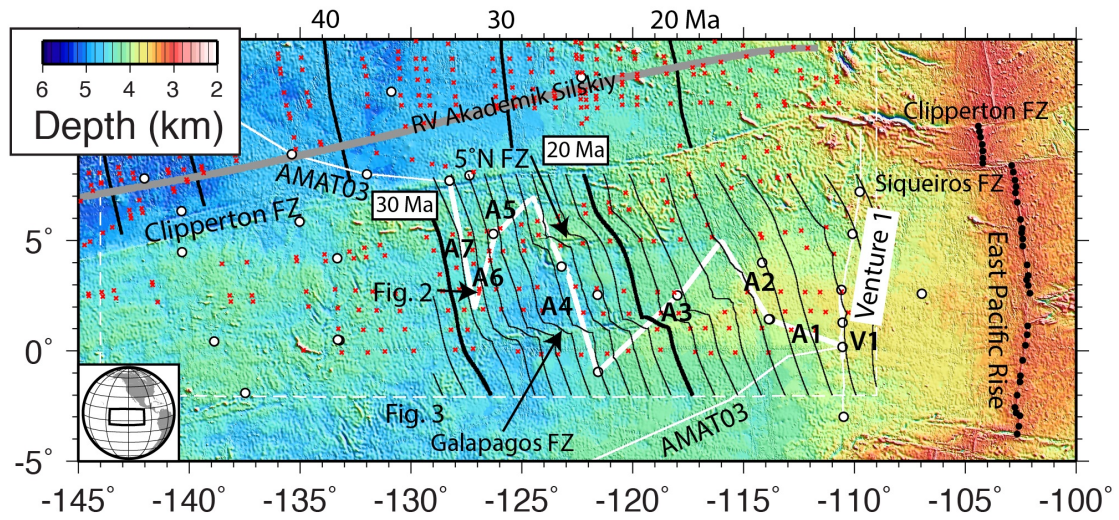
b:
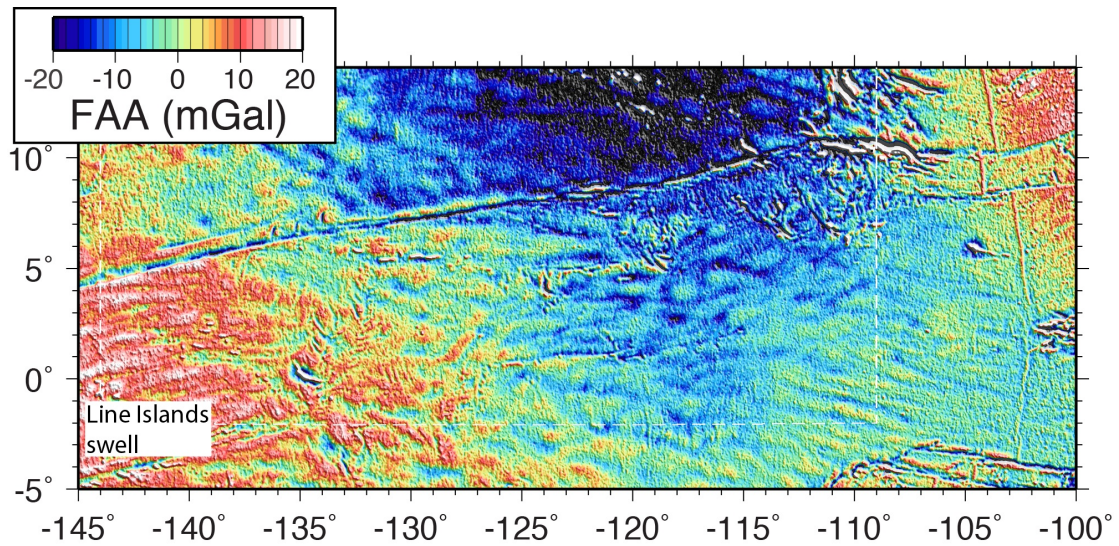
Figure 2. (a) Bathymetry of the central equatorial Pacific (Ryan et al. 2009) along with (white lines) ship tracks for cruises AMAT03 (RV *Revelle*) and Venture 1 (RV *Washington*) and (grey line) RV *Akademik Selskiy*. Tracks are shown in bold where seismic data were interpreted. Bold annotation V1 and A1 to A7 locate segments of the tracks referred to in the text. Red crosses are magnetic anomaly locations of Barckhausen et al. (2013) and solid black contours are crustal ages every 1 m.y. derived from them (bold contours every

10 m.y.). Small solid circles along the East Pacific Rise locate sampled axial

depths shown in Figure 7. Open circles represent scientific drilling sites. "FZ"

represents "fracture zone". (b) Free-air gravity anomalies of the central

equatorial Pacific derived from satellite altimetry measurements (Sandwell et al.

2014) (their version 23).
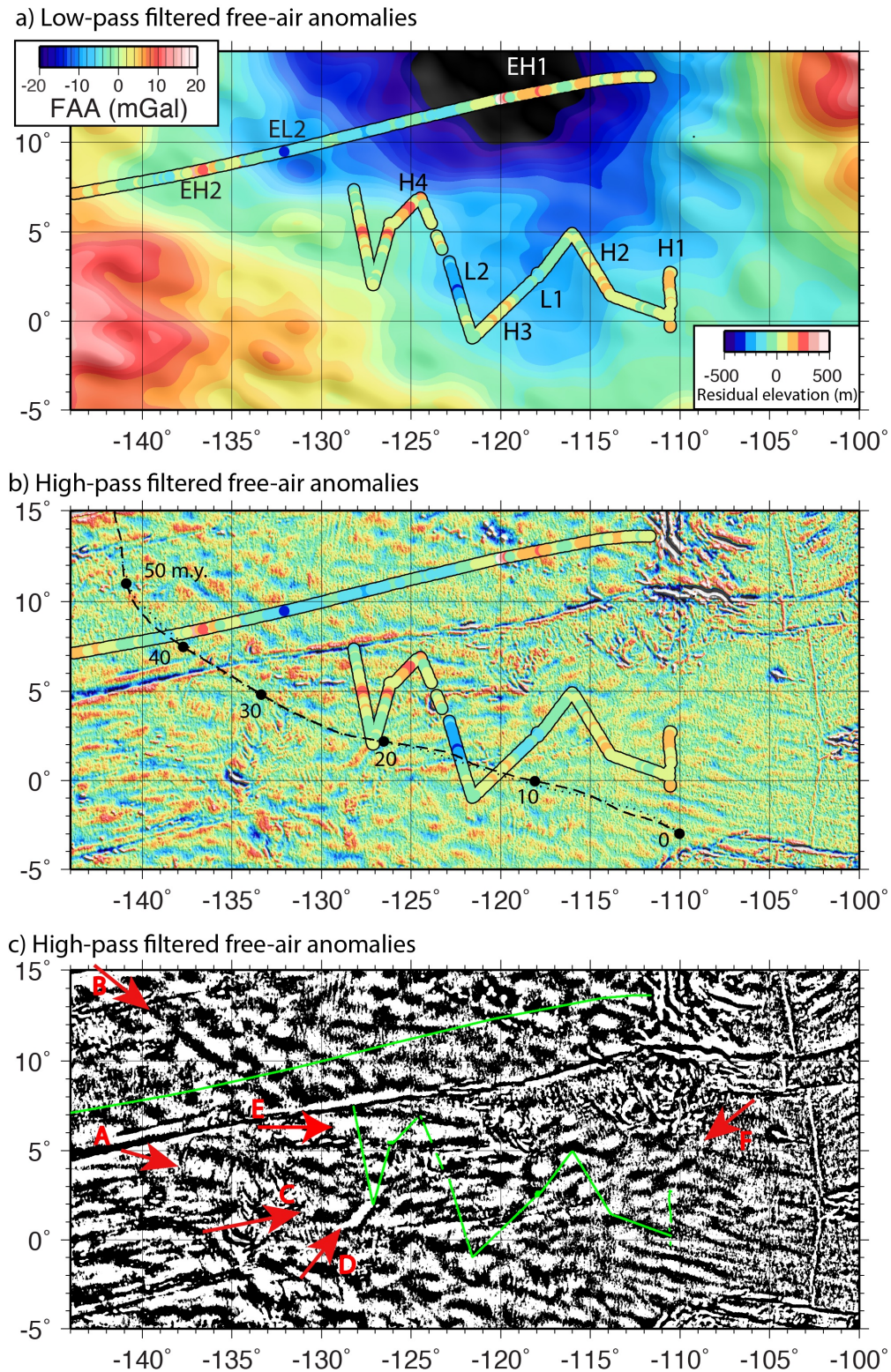
Figure 3. (a) Free-air gravity anomalies of Figure 2b filtered with a 400-km wide cosine-weighted filter (Wessel and Smith 1991) highlighting anomalies with a likely deep (mantle) source. Also shown along the ship tracks here and in (b) with the colour scale lower right are residual elevations representing the

deviations of the basement elevations (corrected for sediment isostatic loading)

from the regressions in Figures 7 and 8. (b) High-pass free-air anomalies

obtained by subtracting the filtered anomalies in (a) from the anomalies in

Figure 2b, effectively representing anomalies more likely arising from basement

and seabed topography and crustal density variations (anomaly scale as in (a)).

Dashed and dotted lines are flow-line reconstructions from a point at 110˚W, 3˚S

using the WK08-G and WK08-A models of Wessel and Kroenke (2008), with

every 10 m.y. marked with closed circles. (c) As (b) though shown with high

contrast to highlight trends. FAA <-5 mGal is shown black, FAA>5 mGal in white

and -5 mGal<FAA<5 mGal in mid-grey. Green lines show seismic cruise tracks.

Red arrows annotated "A"-"F" indicate different lineament trends in this map

that are discussed in the text.
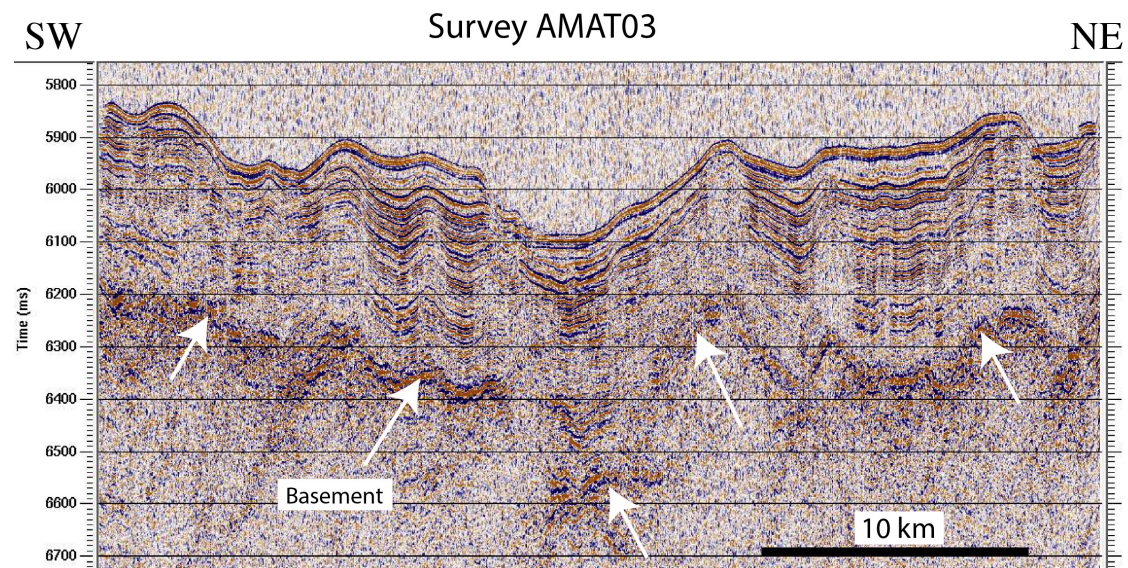
Figure 4. Example of AMAT03 seismic reflection data with basement marked

(white arrows). Survey line is marked in Figure 2a.
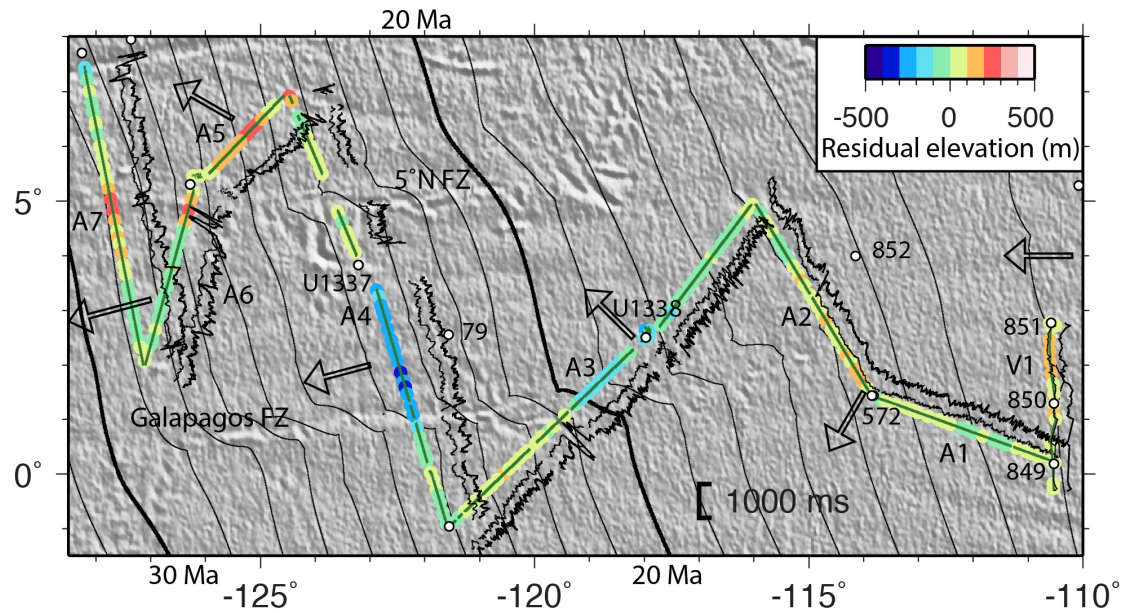
Figure 5. Interpreted seabed and basement reflection two-way times from

Revelle cruise AMAT03 (Dubois and Mitchell 2012). For each line, reflection

times are plotted with fixed directions, as indicated by the open arrows, and with

the scale shown by the 1000 ms scale bar (after subtracting a 5000 ms offset).

Basement is in bold. Also shown along the ship tracks with the colour scale

shown upper-right are residual elevation representing the deviation of the

basement elevation (corrected for sediment isostatic loading) from the

regression in Figure 7.
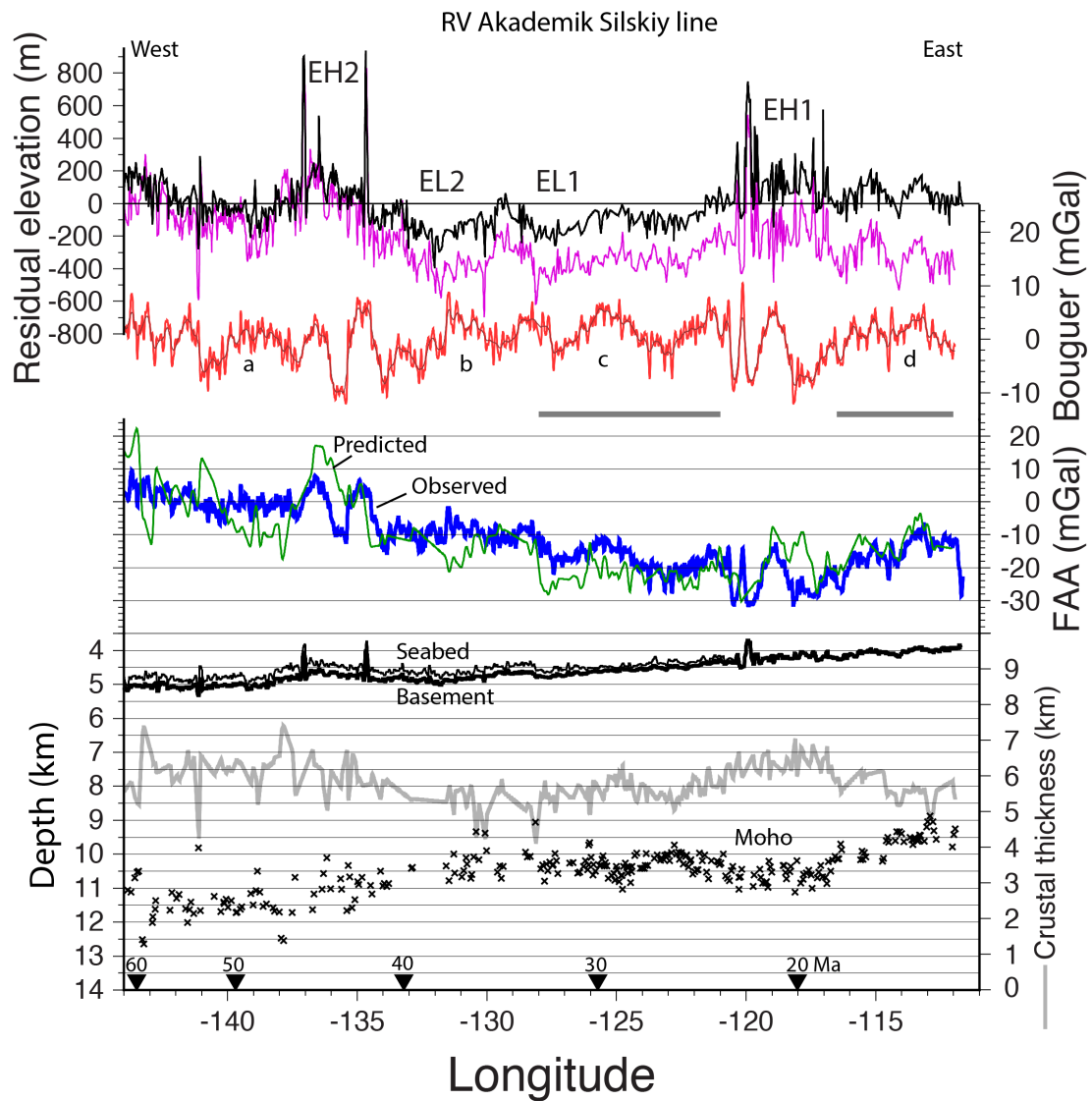
Figure 6. In lower panel, depths of seabed (light line), basement (bold line) and Moho (cross symbols) reflections along the *Akademik Selskiy* line (Figure 2a) are shown, along with crustal thickness (grey line, scale to right). Crustal ages given along the base of the graph are from Müller et al. (2008). Middle panel shows (blue line) free-air gravity anomalies (FAA) derived from satellite altimetry measurements (Sandwell et al. 2014) and (green line) model anomalies derived using the gravity slab formula. In upper panel, red line shows Bouguer anomalies with long wavelength variations removed. Black line shows residual elevations relative to the subsidence trend in Figure 8, while pink line shows

residual elevations calculated allowing for crustal thickness variations as

Hoggard et al. (2017). EH1, EH2, EL1 and EL2 are highs and lows in residual

elevations mentioned in the main text. Grey bars highlight two segments with

somewhat straightforward correlations between Bouguer and residual elevation.
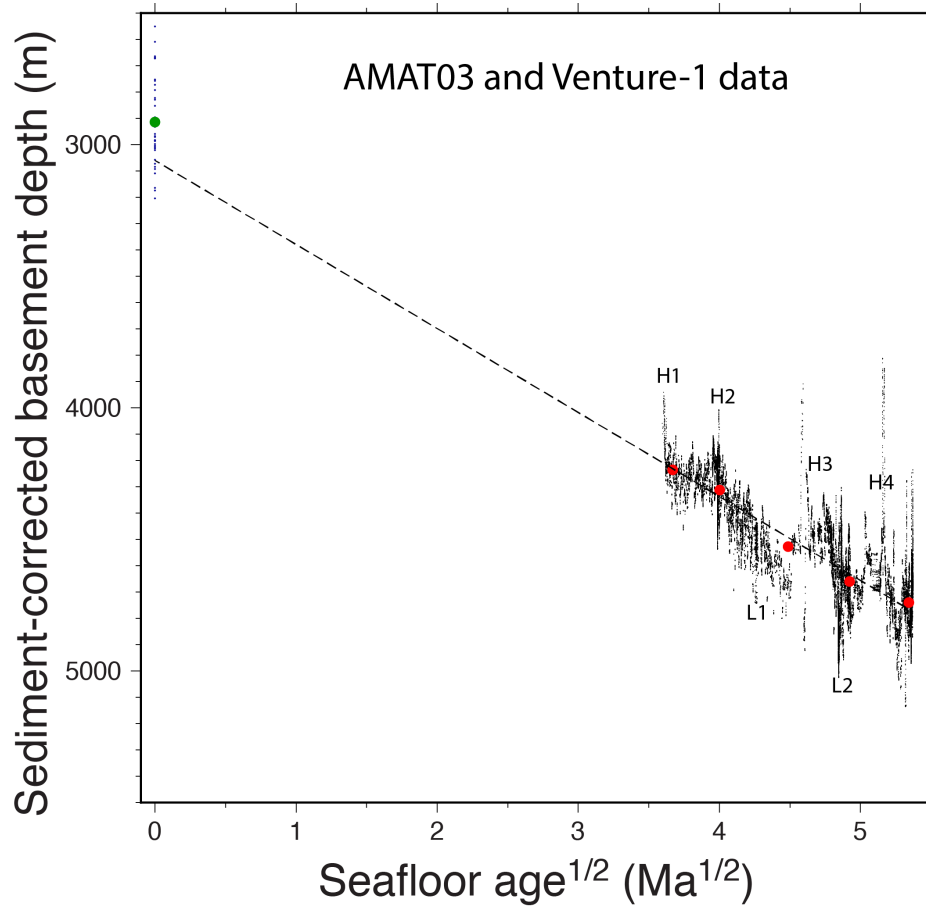
Figure 7. Depth of basement versus square root of crustal age for the data in

Figure 5, with ages based on identifications of Barckhausen et al. (2013). Points

represent individual seismic horizon picks and red circles represent their

averages computed every 0.5 m.y.$^{1/2}$. Dashed line is a simple least-squares

regression through the full seismic dataset (not averages). Annotation L1, L2

and H1-H4 represent areas of residual elevation lows and highs referred to in the

text. Blue dots at zero age are EPR depths sampled from the bathymetry data as

shown in Figure 2a and green circle is their average. These EPR depths were not

used in the regression but are shown to highlight the offset at zero age.
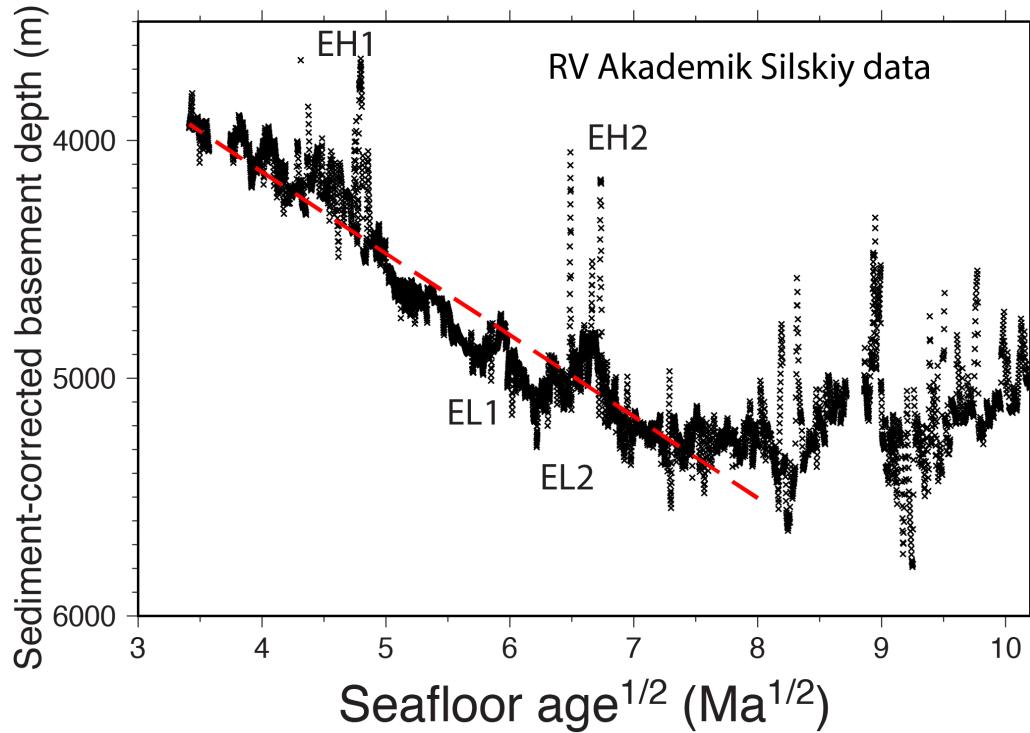
Figure 8. Subsidence trend of basement depth in the RV *Akademik Selskiy*

seismic reflection data (Eittreim et al. 1994) located in Figure 2a. Crustal age

was derived from the isochrons of Barckhausen (2013) and global age grid of

Müller et al. (2008) (their version 3.6). Dashed red line is least squares

regression fitted to the data over the range shown.

a:
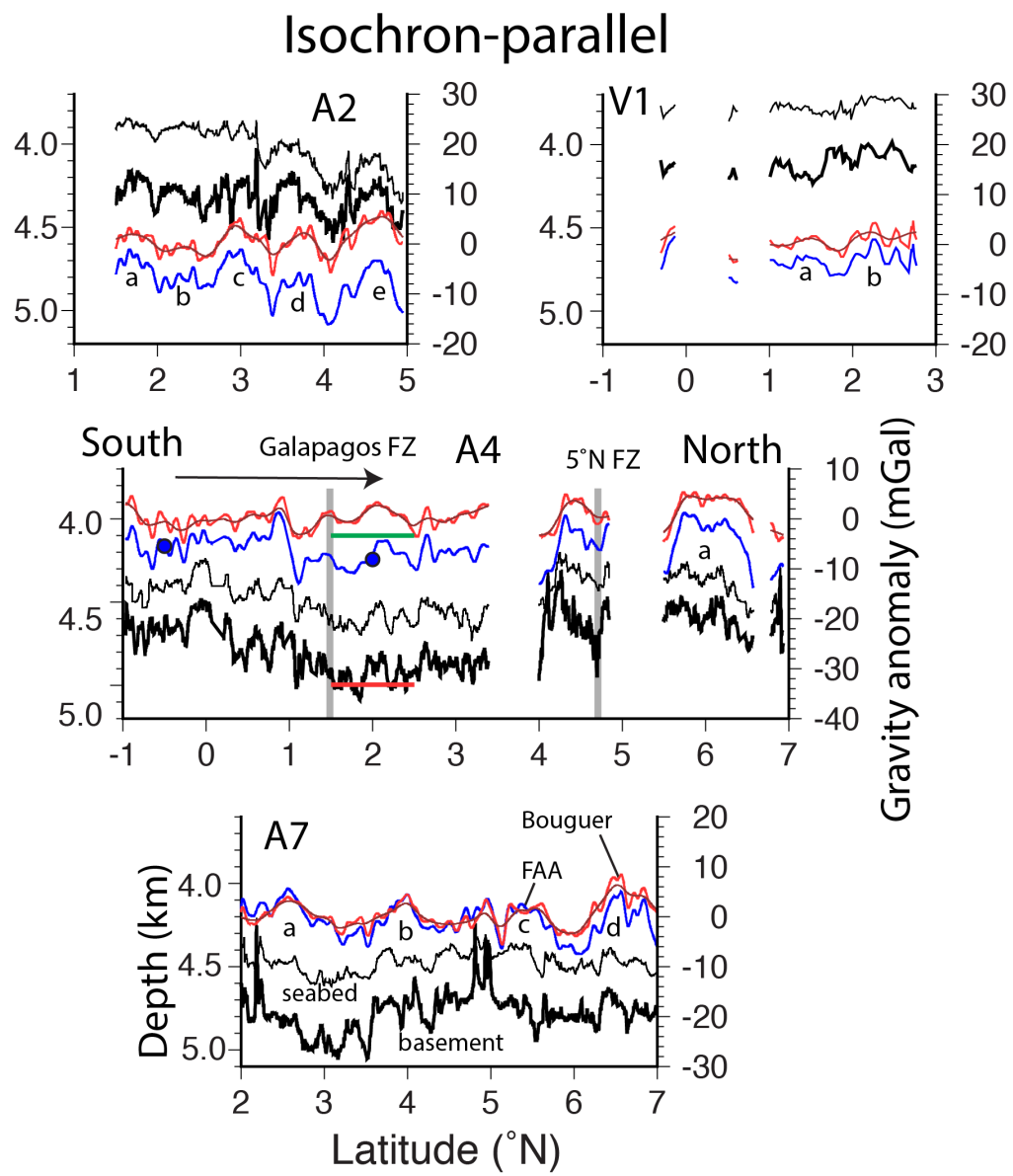
b:
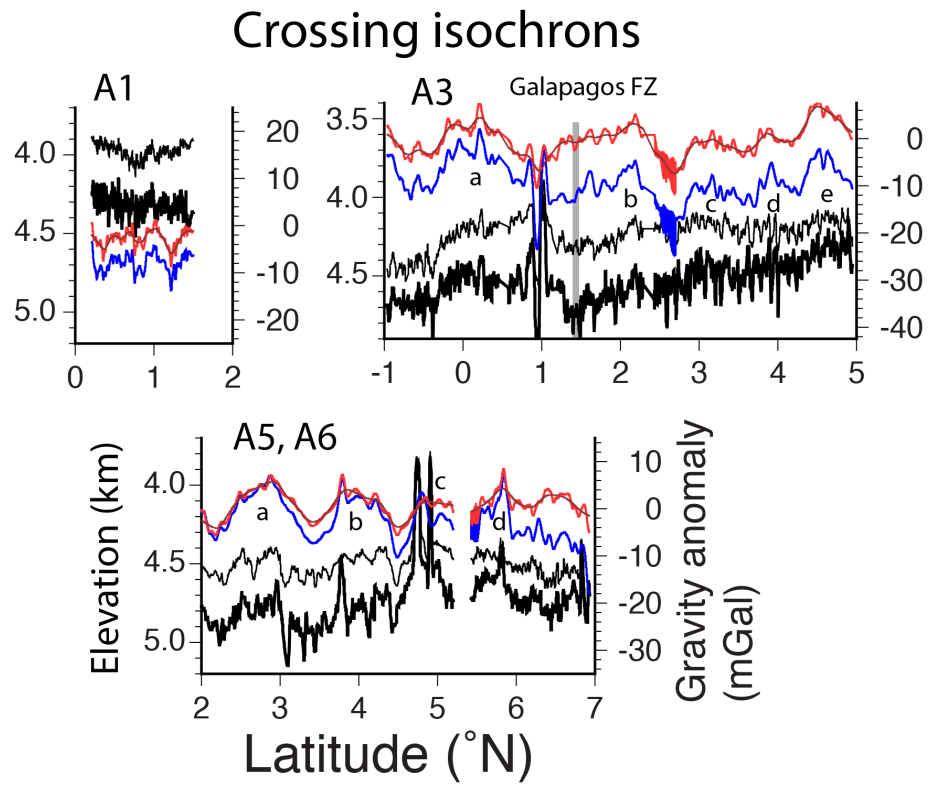
Figure 9. Profiles of seabed and basement elevation (black lines) and free-air gravity anomaly (FAA, blue) and high-pass filtered Bouguer gravity anomaly (red) located in Figure 2a: (a) parallel to crustal isochrons and (b) crossing isochrons. Fine dark red line shows those Bouguer anomalies smoothed with a 50-km wide cosine-tapered filter. Annotation "a", etc., refer to FAA peaks discussed in the text. In graph for A4, blue solid circles represent averaged FAA for -1° to 0° and 1.5° to 2.5°N. In that graph, horizontal bars are FAA predicted at 1.5° to 2.5°N from the change in bathymetry and basement from -1° to 0° for Airy compensated topography (green) and topography not locally supported (red).
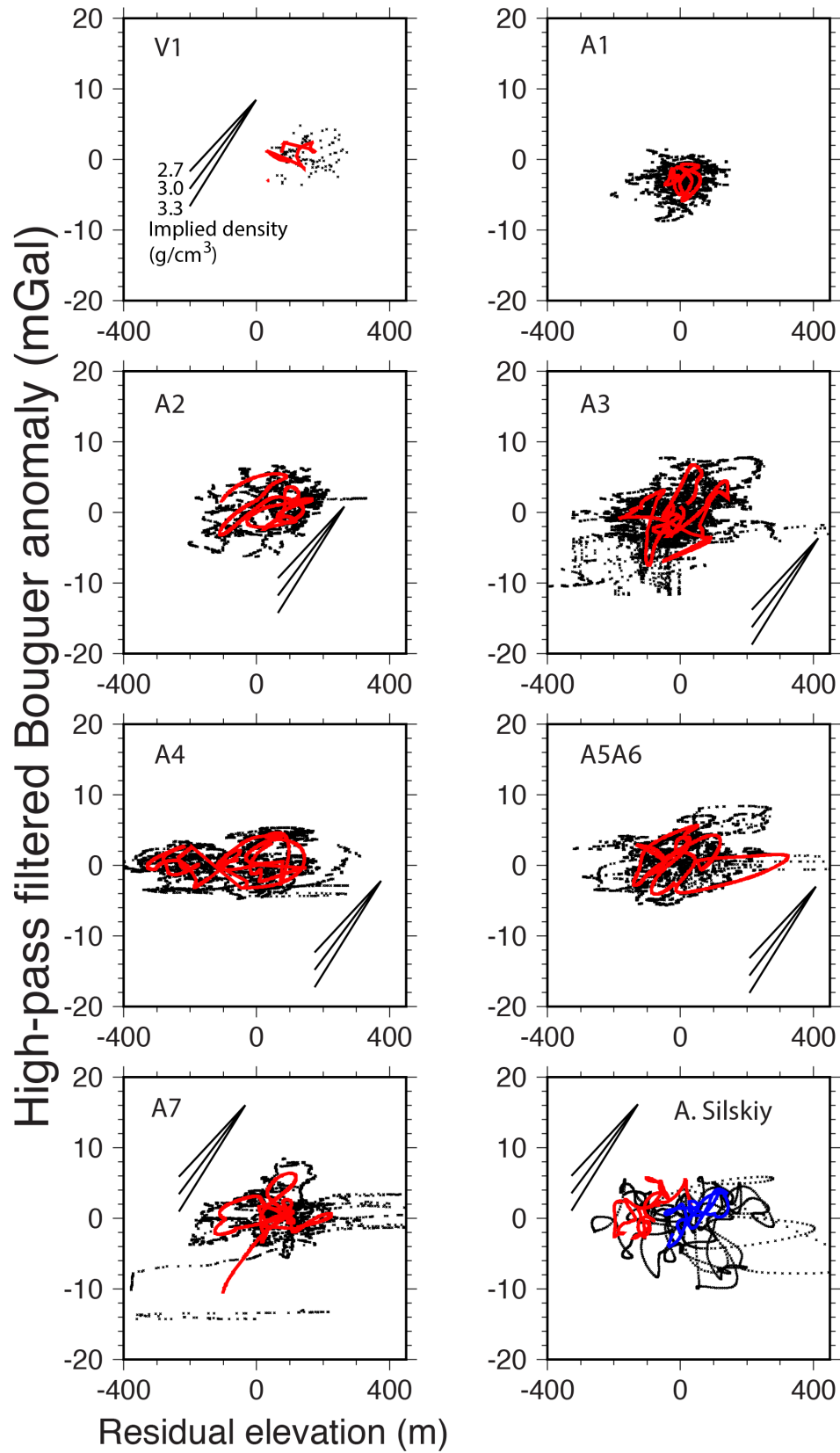
Figure 10. Variation in high-pass filtered Bouguer anomaly with basement

residual elevation for the various seismic lines (marked in upper-left of each

panel). "A. Silskiy" represents the RV *Akademik Silskiy* line. Overlain in red for

V1-A7 are the data shown after a 50-km cosine-tapered filter was applied to

remove short wavelength fluctuations. All data for the *Akedemik Silskiy* data

have this filter applied. Red and blue in that panel show data corresponding to

the extents of the two grey bars in Figure 6. Three lines in upper-left panel and

reproduced in other panels show the trends to be expected if gravity-elevation

changes were due to a single interface between sediment (1.5 g cm^{-3}) and the
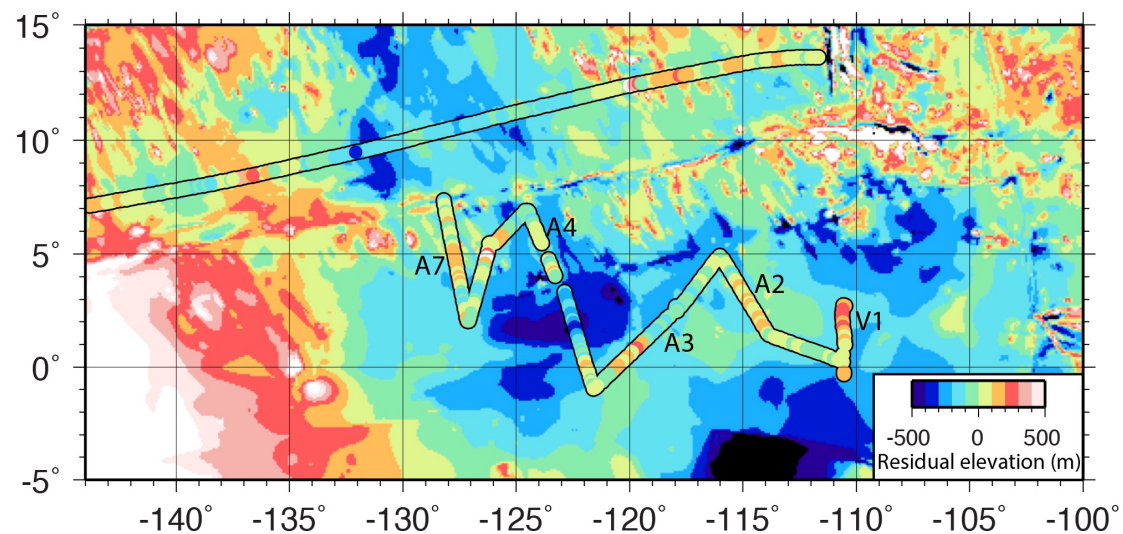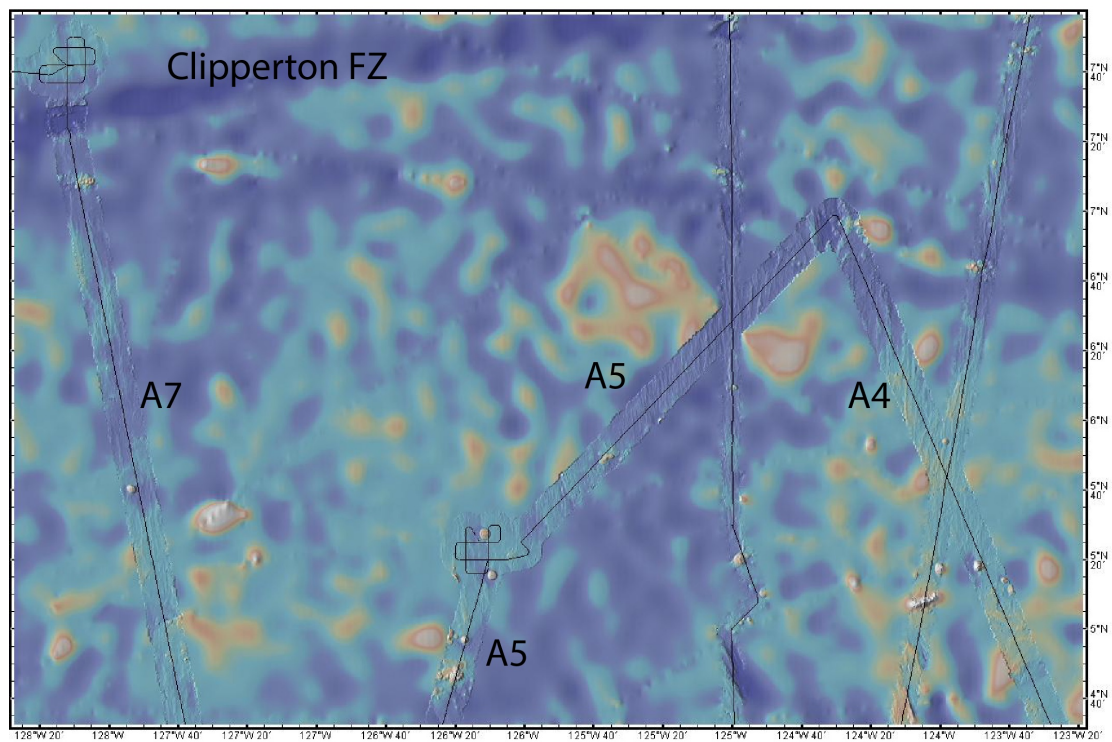
density shown.

Figure 11. Residual elevations derived here from the seismic reflection datasets

compared with those of Crosby et al. (2006).

a) NW area with seamounts
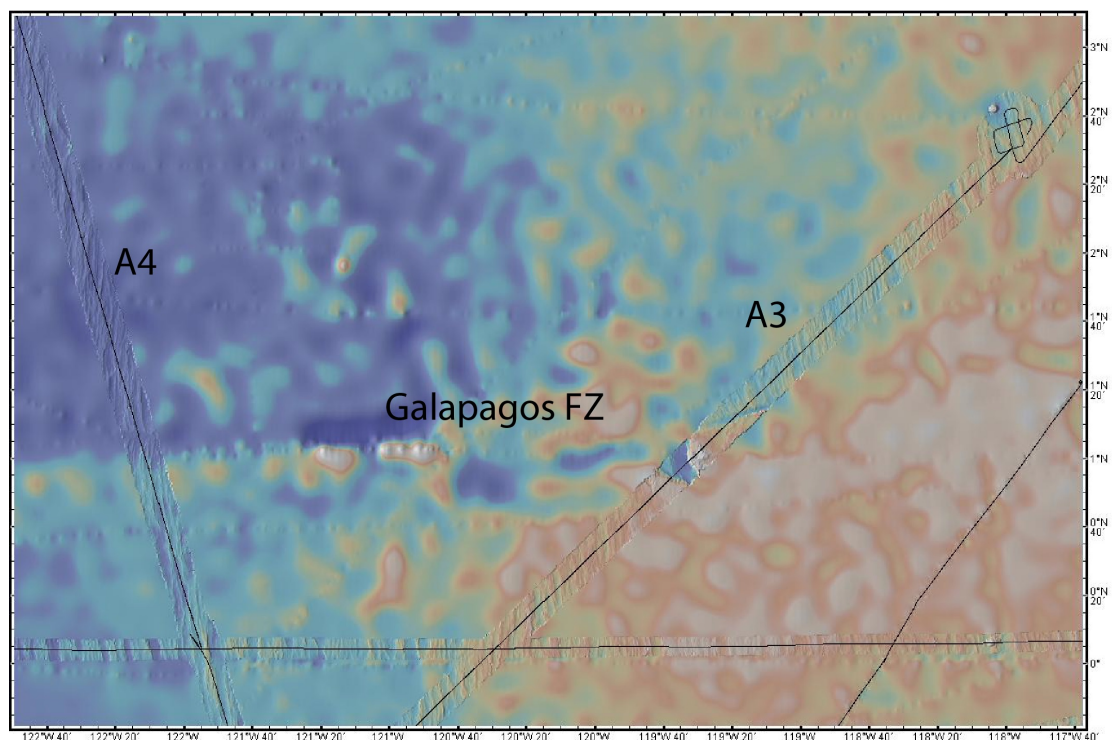

b) SE area with few seamounts

Figure 12. Examples of bathymetry data from multibeam sonars incorporated in the Ryan et al. (2009) dataset (maps created using the GeoMapApp data browsing tool (www.geomapapp.org)). (a) Area adjacent to Clipperton FZ

including northern parts of lines A4-A7 showing region of small seamounts. (b)

Southern area encompassing the Galapagos FZ with few seamounts. In both

panels colours from dark blue to white correspond to 4800 to 3800 m depths

and illumination is from N80°W. Multibeam data lie about tracks marked with

solid black lines, whereas other lower-resolution bathymetry in each map was

derived from satellite altimetry or sparse single-beam echo-sounder data (Ryan
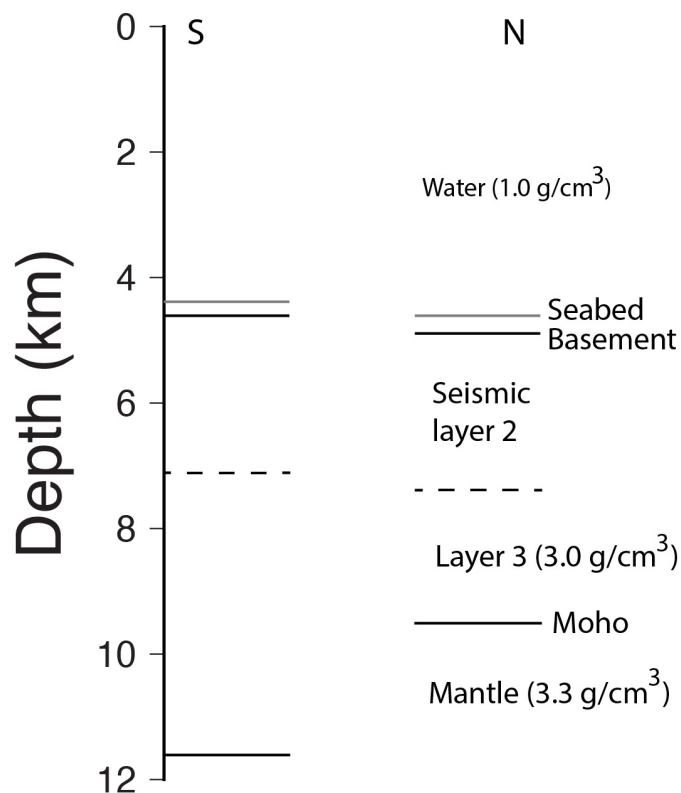
et al. 2009).

Figure 13. Illustration of the estimated change in Moho depth resulting from

local compensation of the change in basement depth on crossing the Galapagos

Fracture Zone along line A4 in Figure 9a.